



Effect of crystal phase composition on the reductive and oxidative abilities of TiO_2 nanotubes under UV and visible light

Kevin L. Schulte^a, Paul A. DeSario^b, Kimberly A. Gray^{b,*}

^a Department of Chemical and Biological Engineering, Northwestern Univ., Evanston, IL 60208, USA

^b Department of Civil and Environmental Engineering, Northwestern Univ., Evanston, IL 60208, USA

ARTICLE INFO

Article history:

Received 23 September 2009

Received in revised form 7 April 2010

Accepted 15 April 2010

Available online 22 April 2010

Keywords:

Titanium dioxide

Nanotubes

Carbon dioxide reduction

Acetaldehyde oxidation

ABSTRACT

Titania nanotube arrays synthesized by the electrochemical oxidation of titanium foils have generated considerable interest as photocatalysts for their ordered nature and large surface area. Mixed-phase materials combining the anatase and rutile crystal phases of TiO_2 , however, have been much more widely studied due to their enhanced reactivity in comparison to pure phase materials. In this study, we seek to integrate these two lines of research and investigate the reductive and oxidative reactivity of TiO_2 nanotube arrays (anatase phase) supported on TiO_2 films of varying crystal phase composition. A series of TiO_2 nanotubes 1.2 μm in length was synthesized, annealed at varying temperatures to control their crystallinity, and characterized by various physical techniques (e.g. XRD, diffuse reflectance, SEM). Photocatalytic CO_2 reduction and acetaldehyde oxidation reactions were performed in the gas phase under UV and visible wavelengths. For CO_2 reduction, reaction rates decreased with increasing rutile phase under UV. Rates increased with rutile phase ratio under visible and near visible light. For oxidation, the mixed-phase samples showed enhanced reactivity, with a maximum acetaldehyde destruction rate achieved at a 79:21 ratio of anatase to rutile. The samples were substantially less active under visible light, except for the 620 °C composite (77% rutile) which showed a slight rate increase. Nanotubes annealed at 680 °C collapsed to a random porous structure, but showed comparable reductive ability to the non-collapsed samples despite the loss of surface area. This is attributed to the creation of additional anatase–rutile crystallite interfacial area leading to the formation of unique active sites. Control of crystal phase composition through anneal temperature is found to be a simple way to tune the reactivity of these materials and enhance their ability to absorb visible light.

© 2010 Elsevier B.V. All rights reserved.

1. Introduction

TiO_2 is widely studied as a photocatalyst due to its strong redox properties, low cost, chemical stability and non-toxicity. Numerous applications for TiO_2 have been discovered: chemical transformations [1–3], destruction of pollutants [4,5], disinfection [6], gas sensing [7,8], and self-cleaning surfaces [9,10], to name a few. The discovery of self-organized TiO_2 nanotube (TiNT) arrays formed by electrochemical synthesis by Grimes and co-workers [11] has opened new avenues in TiO_2 research. TiO_2 nanotubes have promoted intriguing research due to their enhanced surface area, ordered geometry and tunable morphologies [12]. TiNTs have displayed enhanced performance compared to other forms of TiO_2 as electrodes for dye sensitized solar cells [13,14], gas sensors [15], and photocatalysts [16].

Two catalytic applications of TiNTs under current investigation are (1) the oxidation of organic compounds in various media (photocatalytically in the gas [17,18] and aqueous [19–22] phases and photoelectrochemically [23,24] in the aqueous phase) and (2) the photoreductive reforming of CO_2 into energy containing hydrocarbons such as methane [25]. The former technology is promising for air purification through the degradation of volatile organic compounds in the air, such as acetaldehyde [17]. The latter could be employed by high carbon emissions industries (e.g. coal fired electricity generation) to convert a waste product to a valuable fuel or chemical feedstock, or as a means of resource recovery within a production cycle.

The most abundant crystal phases of TiO_2 are anatase and rutile. Anatase has a wider band gap than rutile (3.2 eV vs. 3.0 eV) [26], but it is regarded as the more reactive phase due to improved hole trapping resulting from steeper band bending [27,28]. In contrast, the relatively shallow band bending of rutile results in rapid charge recombination and highly reduced photocatalytic activity [29,30]. Numerous reports have shown that mixed-phase TiO_2 formulations display enhanced reactivity and improved visible photoresponse compared with pure phases [30–34]. These

* Corresponding author at: Department of Civil and Environmental Engineering, Northwestern University, 2145 Sheridan Rd., Rm A236, Evanston, IL 60208, USA. Tel.: +1 847 467 4252; fax: +1 847 491 4011.

E-mail address: k-gray@northwestern.edu (K.A. Gray).

enhancements are attributed to improved charge separation and hindered charge recombination by electron transfer from rutile to anatase at the interface between the two phases [26,30] coupled with the extended photoresponse of rutile. Also, there is evidence that the interface between rutile and anatase crystallites creates defect sites with unique adsorption and charge trapping properties that contribute to high reactivity at these interfaces [35,36]. In fact, catalytic “hot spots” are thought to be associated with interfacial undercoordinated Ti^{4+} (e.g. tetrahedral coordination) [26] and oxygen deficiencies [37]. To the best of our knowledge, no study has investigated if these mixed-phase features can be integrated into TiNT arrays in order to enhance the redox activity of the material in the gas phase (particularly under visible light).

It has been shown that it is possible to control the crystalline composition of nanotube arrays through the choice of the annealing temperature [38]. The nanotube arrays electrochemically anodized in Ti foil consist of TiO_2 nanotubes atop a thin TiO_2 layer on the foil [38]. The nanotubes are amorphous as prepared and begin to crystallize as anatase around 280 °C. The geometrical limits imposed by the nanotube walls prevent rutile nucleation at higher anneal temperatures due to the stability of the small anatase crystallites [39] and the inability of the crystallites to attain the proper orientation required for rutile growth [40]. Rutile begins to appear around 430 °C and only forms in the oxide barrier layer to which the nanotubes are attached [12,38].

The aim of this work is to analyze the reductive and oxidative reactivity of TiNT arrays as a function of their crystal phase composition with the goals of enhancing reactivity and extending the visible response of these materials. In order to do this, a series of otherwise identical nanotube arrays was synthesized with varying ratios of the anatase and rutile crystal phases of TiO_2 . The crystallinity and light absorption properties were characterized and the relative abilities TiNT to oxidize acetaldehyde and reduce CO_2 were compared under varying light energies.

2. Experimental

2.1. Catalyst synthesis

Nanotube arrays were synthesized by electrochemical anodic oxidation similar to the method outlined by Cai et al. [12]. The two electrode system consisted of a Ti foil anode and a platinum wire cathode connected to a power supply. The electrolyte bath contained 1 M H_2SO_4 and 0.8 M KF adjusted by pelletized NaOH to a pH of 4.0 as measured by a bench top pH/mV/°C meter (Cole Parmer). Ti foils (Alfa Aesar) of 0.0127 mm thickness were cleaned by sonication in acetone for 10 min prior to anodization then rinsed in deionized water and dried in air. All anodizations were performed at 20 V for 2 h with mild agitation provided by a magnetic stir bar, resulting in nanotubes about 1.2 μm in length with between 80 and 100 nm inner diameter. After anodization, samples were removed from the electrolyte bath, cleaned by brief sonication in water and then dried in air.

2.2. Catalyst characterization

The nanotube films are amorphous as prepared, and must be annealed at high temperatures to induce crystallinity. Annealing was performed in a Thermolyne 62700 muffle-furnace in ambient air at a rate of 1 °C/min up to the target temperature, where it was held constant for 6 h. The furnace was then turned off, and the samples were allowed to cool with the furnace door closed for 3 h. A Rigaku D/Max-A X-ray diffractometer, featuring a sealed Cu X-ray tube and scintillation detector, was used to determine sample crystallinity. Samples were analyzed under a Hitachi S-4800

Table 1
Total irradiance for the lamp sources used in this study.

Lamp source	Irradiance (W/m ²)
Hg vapor (365 nm)	113.5
Xe arc, 380 nm filter	34.5
Xe arc, 400 nm filter	15.9

scanning electron microscope and images were acquired via Quartz PCI software. Analysis of intact and mechanically cracked samples allowed for precise measurement of morphological properties such as diameter, and tube length. Photoabsorbance measurements were obtained using a Perkin Elmer Lambda 1050 UV/Vis/NIR spectrophotometer equipped with a 150 mm InGaAs integrating sphere.

2.3. CO_2 photoreduction experiments

CO_2 photoreduction experiments were conducted in a sealed 17.5 mL Teflon reaction chamber with a quartz window that allows all radiation of wavelength >300 nm to pass. CO_2 entering the chamber first passed through an H_2O bubbler where it was saturated with deionized water. Before starting a reaction, the humid gas was purged through the reaction chamber with the catalyst sample inside for 30 min. At the same time, a heating plate was turned on to set the desired reaction temperature of ~90 °C. When purging was complete, the reactor was sealed and a pump was turned on to circulate the reaction gases through the chamber at a rate of 6 mL/min. At this point, the irradiation source was placed over the quartz window, initiating the reaction.

Two different types of light sources were used: (1) a Blak-Ray™ long wave UV lamp with a 100 W mercury vapor bulb with 365 nm emission and (2) an Oriel model# 66921 lamp housing with a 1000 W Xe arc lamp (6269) that has a flat broad spectrum from UV to infrared wavelengths. The Oriel lamp was equipped with a 3.8-cm f/1.0 lens, with a water filter attachment to absorb infrared radiation. Oriel bandpass (5 cm) light filters were used to limit the radiation to a narrow range centered at the target wavelength. 380 and 400 nm filters with ~14 nm bandwidth at 10% transmittance and ~20 nm at 1% transmittance were used. These lamp sources (365, 380, and 400 nm) were chosen with the bandgaps of rutile (410 nm) and anatase (385 nm) in mind, allowing for selective activation of the anatase and rutile phases. The light intensity from each of the various sources was quantified with an Apogee Instruments PS-100 spectroradiometer with half nanometer bandwidth resolution, held beneath the lamp source behind a quartz window at the same distance as the catalyst sample would be inside the reactor. Irradiance values for each lamp source are listed in Table 1.

Reaction gases were analyzed with a HP 4980 series II gas chromatograph (GC) featuring a Porapak Q separation column and a flame ionization detector (FID). Output from the detector was received and integrated by an Agilent 3396 Series III integrator.

2.4. Acetaldehyde oxidation experiments

Acetaldehyde oxidation reactions were performed in the same reaction chamber utilizing the same irradiation sources as before, but with no reactant circulation. Also, experiments conducted under the Blak-Ray™ lamp were performed at room temperature while those under the filtered Oriel lamp were conducted at 48 °C to increase degradation rates.

Before beginning a reaction, the chamber containing the catalyst sample was purged with humid O_2 for 30 min. At that point, the reaction chamber was sealed and 40 μmol of acetaldehyde gas was injected inside the dark chamber. The acetaldehyde was allowed to achieve adsorption equilibrium (typically 45 min) at which point

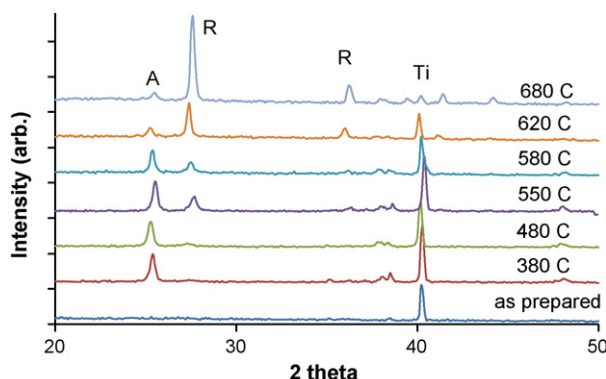


Fig. 1. XRD Spectra of samples annealed at varying temperatures. All samples were synthesized under the same conditions (pH 4.0, 20 V, 0.8 M KF, 2 hr anodization) and are ~1.2 micron in length.

the reactor was illuminated. Reaction gases analyzed by gas chromatography.

3. Results and discussion

3.1. Effect of anneal temperature properties

The XRD spectra of the nanotube samples are presented in Fig. 1. As expected, the sample as prepared was completely amorphous and only the Ti peak (~40°) is present. The sample annealed at 380 °C exhibited pure anatase crystallinity. At 480 °C, the first traces of rutile appear indicating that the barrier oxide layer below the nanotubes is beginning to convert to the rutile phase. The relative intensity of the rutile peak continues to increase with increasing temperature as the oxide layer becomes fully converted to rutile at 620 °C. The intensity of the Ti peak (~40°) relative to the TiO₂ peaks remained relatively constant until somewhere between 580 and 620 °C. At this point, the Ti intensity began to decrease, accompanied by a rapid increase in rutile intensity. This reduction in the Ti signal indicated that, at this point, atmospheric O₂ was diffusing through the oxide layer and oxidizing the remaining Ti substrate. This must be the case because at 620 °C, the rutile peak intensity was greater than the anatase even though the nanotubes (which must be anatase) remained in tact. New rutile must be forming to cause that increase in intensity. At 680 °C, the relative intensity of the anatase peak is greatly diminished compared to the intensity of the rutile peak. This anneal temperature corresponds to the temperature at which the nanotube structure collapses and the anatase in the nanotubes finally begins converting to rutile.

From the XRD data, we calculated the relative amounts of anatase and rutile crystallites that are present using the Spurr equation [41]:

$$F_R = \left[\frac{1}{1 + 0.78(I_{A(101)}/I_{R(110)})} \right] \times 100\% \quad (3.1)$$

where F_R is the percent by weight of rutile phase in an mixture of anatase and rutile, $I_{A(101)}$ is the integrated peak intensity of the anatase (101) face and $I_{R(110)}$ is the integrated intensity of the rutile (110) face. Through the integration of the spectra in Fig. 1, the crystal phase composition achieved as a function of anneal temperature was determined. Also, the derivative of this function was estimated by plotting the slope between each set of consecutive points at their midpoint. These calculations are plotted in Fig. 2. The rate of rutile phase formation begins slowly between 380 and 480 °C, increases with temperature reaching its highest point around 600 °C where atmospheric O₂ is oxidizing the Ti substrate. This rate levels off as almost all of the anatase phase is converted

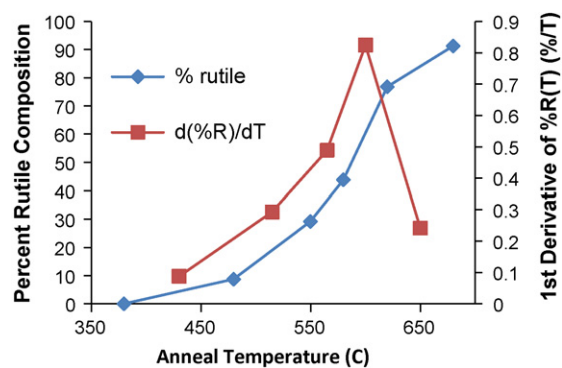


Fig. 2. Crystal phase composition as a function of anneal temperature, as calculated by Spurr's equation. The first derivative of this function is also plotted showing the change in rutile composition with temperature.

to rutile at 680 °C. These data clearly illustrate that phase composition of the oxide layer can be readily tuned by anneal temperature. While the nanotubes are always constrained to the anatase phase, the oxide layer transitions from amorphous, to anatase, to a mix of anatase and rutile and finally to pure rutile as anneal temperature is increased.

As for the tube morphology observed by SEM, annealing between 0 and 620 °C does not appreciably affect the nanotubes, but the tube samples annealed at 680 °C collapse into a more random porous structure (Fig. 3). This is consistent with what is known about the mechanism of nanotube crystallization. During annealing, the nanotubes remain anatase even at high temperatures, due to the constraints placed by the tube walls on nucleation of the larger rutile crystals [12,38]. This condition persists until somewhere between 620 and 680 °C, where there is enough energy to cause the tube walls to rupture and allow the formation of the larger rutile crystallites. This is confirmed by the XRD scan of the 680 °C sample (Fig. 3), which is almost completely rutile. Varghese et al. [38] also observed a similar behavior in nanotube structure with temperature.

Shown in Fig. 4 are the UV-vis spectra of the nanotube samples. In general, the UV absorbance of the NT samples decreases with increasing anneal temperature. At the same time the visible light absorbance slightly increases and shifts slightly towards red wavelengths as more rutile phase is introduced. Overall, the curves appear to flatten out over the range 250–400 nm. The increase in visible absorbance is attributed to the increased rutile content at higher anneal temperatures.

The 620 and 680 °C samples (which are both over 75% rutile) show two absorption bands, which can be attributed to the relative absorbances of each phase (385 and 410 nm for bulk anatase and rutile, respectively). These absorbances are blue-shifted compared to the bulk values, which can be explained by the decreased density of states in the nanostructured TiO₂. The samples between 480 and 580 exhibit only one major absorbance component, even though they contain rutile. This may indicate a shift in the interaction between the two phases.

This trend is confirmed in Fig. 5 which compares the band gap energies calculated by extrapolation of the absorbance edge. These data suggest that the band gap energy is decreasing with increasing anneal temperature (and by extension, increasing rutile content). Annealing at 380 °C results in a pure anatase sample that has a band gap of 378 nm. This value is below the typical anatase band gap of 385 nm, confirming the blue shift associated with nanoparticles. The sample annealed at 680 °C which is over 90% rutile has a calculated band gap of 409 nm, which is very close to the literature value of 410 nm for rutile. This demonstrates that anneal temperature allows for the synthesis of mixed-phase catalysts with

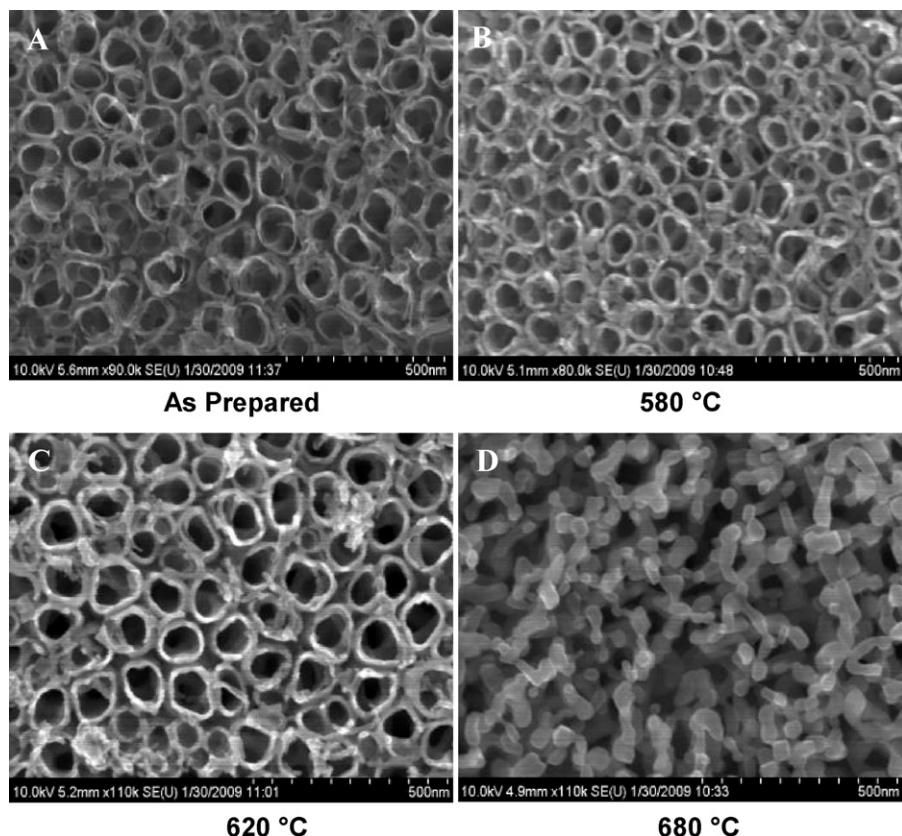


Fig. 3. (A–D) SEM images of samples annealed at various temperatures. At 680 °C, the tubular structure breaks down, leaving a semi porous structure behind. 500 nm resolution.

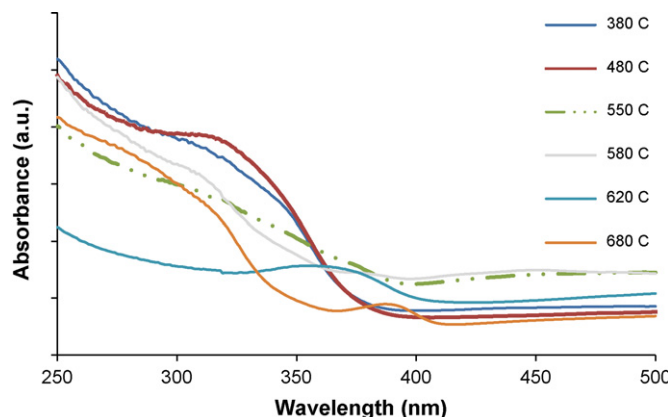


Fig. 4. Absorbance spectra of nanotube samples prepared under identical conditions except for anneal temperature. Generally, UV absorbance decreases with increasing anneal temperature while visible absorbance shows a slight red shift.

an ability to absorb further into the visible portion of the spectrum.

3.2. CO_2 reduction experiments

The results of the CO_2 photoreduction experiments under 365 nm irradiation are illustrated in Fig. 6. The methane production rates per plan area of catalyst are presented as a function of catalyst anneal temperature with the % rutile indicated in parentheses. The 365 nm excitation is energetic enough to excite both the anatase and rutile bandgaps. The 480 and 680 °C samples display the highest methane production under this illumination condition. Since the 480 °C sample is 90% anatase (considered the more active

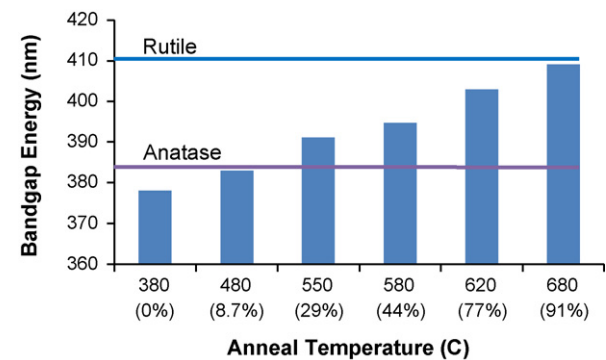


Fig. 5. Band gap energies of TiO_2 nanotube samples as a function of anneal temperature. These energies were calculated by extrapolation of absorbance curves. Also shown are lines denoting the band gap energies of bulk anatase and rutile TiO_2 .

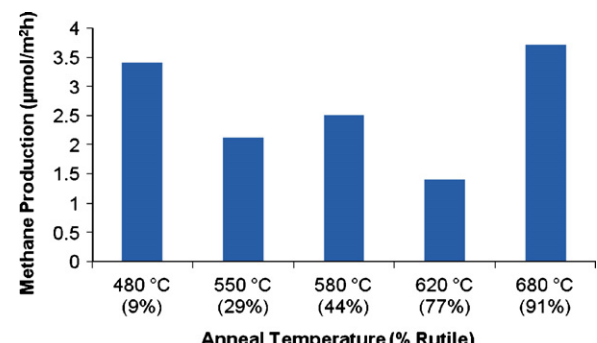


Fig. 6. Methane production under 365 nm irradiation for TiNT arrays of varying anneal temperature. Experiments were conducted in a gas phase batch reactor. The values in parentheses indicate the % rutile content of the arrays.

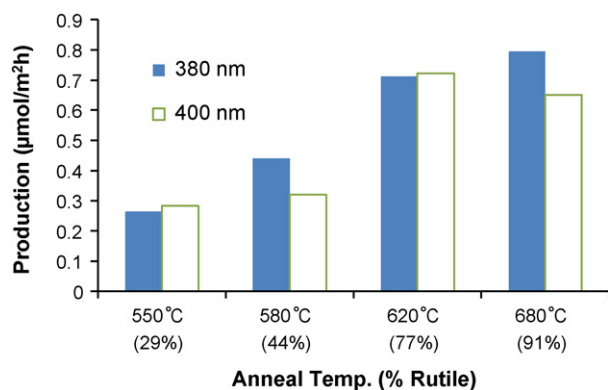


Fig. 7. Methane production under 380 nm and 400 nm irradiation for TiNT arrays of varying anneal temperature.

phase) and has a higher UV absorbance than the other samples (Fig. 4) it follows that it is one of the more active catalysts under 365 nm irradiation. The 620 °C sample is the least reactive at this wavelength, consistent with its lowest UV absorbance. In general, UV methane production decreases with anneal temperature above 480 °C. There is a slight increase for the 580 °C sample (relative to the 550 and 620 °C samples), indicating perhaps a local optimum mixture of phases.

The sample annealed at 680 °C, however, exhibits unique reactivity at this wavelength. As noted before, the nanotubes in this sample had collapsed after annealing at this temperature. Despite this collapse (which is expected to decrease the active surface area), the sample produces methane at a rate similar to that of the 480 °C sample. This heightened activity may be explained by the creation of new active sites that are distinct from those in the other samples. As noted before, the constraints of the tube walls limit the rutile growth to the barrier layer below the tubes, effectively separating the two phases. Hurum et al. [26] and Li et al. [42] noted that highly active catalytic sites form at the anatase–rutile interface, sites consistent with “distorted” regions at the anatase crystallite surface associated with rutile nucleation sites. The collapse of the tube walls is consistent with the creation of more of these sites, which in turn compensates for the diminished surface area of this sample.

Data were also collected for the samples under 380 and 400 nm light to probe visible light activity as a function of anneal temperature/rutile content. While 380 nm would still excite both anatase and rutile, the quantum efficiency of anatase excitation would be much lower, since this wavelength is much closer to the anatase bandgap. The wavelength of 400 nm was chosen to selectively excite the rutile phase and not the anatase phase. Results of these experiments are presented in Fig. 7.

Under 380 nm irradiation methane production is not observed for the 480 °C sample, or samples annealed at temperatures below that. Methane was produced under these wavelengths only by the samples that were annealed at higher temperatures and displayed rutile content in their XRD profiles. This indicates that the rutile content of the oxide barrier layer is critical for visible light activation of the TiNT composite arrays. Among the TiNT samples that do show appreciable methane production, the 680 °C sample retains the highest production (though it no longer has a tubular structure), which is consistent with its high rutile content. The other samples produce methane in the order of their calculated band gaps and also in the order of rutile phase composition.

The methane production for these samples under 400 nm light exhibits a similar trend, with methane production increasing with anneal temperature/rutile content and the methane yield changed only slightly at 400 nm relative to 380 nm. Experiments

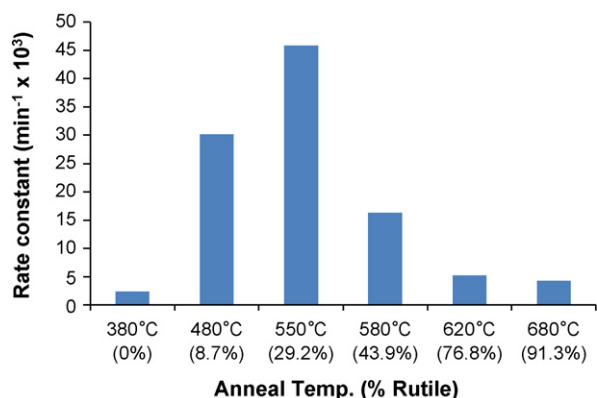


Fig. 8. Acetaldehyde oxidation first order apparent rate coefficients under 365 nm irradiation for TiNT arrays of varying anneal temperature. Experiments were conducted in a gas phase batch reactor.

conducted under 430 nm radiation did not exhibit any reactivity.

3.3. Oxidation reaction results

Data from the acetaldehyde oxidation experiments were fit to a first order rate law for a batch reactor, allowing for the determination of rate constants [17]. The apparent first order rate constants of the acetaldehyde oxidation experiments conducted under 365 nm light are shown in Fig. 8. The 550 °C sample exhibits the highest reactivity with an apparent rate constant of 0.0458 min^{-1} . Under our reaction conditions, complete degradation was achieved after just about 100 min. The 380 °C pure anatase sample displays the lowest reactivity indicating that the presence of at least some rutile greatly enhances the reactivity of the nanotube array. This coincides with previous evidence of the enhanced reactivity of mixed-phase TiO_2 [21,30–33], but in the case of TiNT the mechanism of this improvement for oxidative reactivity may be associated with the evolution of undercoordinated Ti^{4+} species that are the intermediate to the formation of rutile at the anatase nanoparticle interface [42,43]. Since reaction with CO_2 showed a completely different trend, the population of active sites formed with annealing up to 550 °C may be selectively active for acetaldehyde oxidation. Beyond 550 °C, the reactivity decreases with increasing anneal temperature, indicating, as others have found, that there is an optimum ratio of anatase to rutile for acetaldehyde oxidation (71:29 in this case). This is a similar optimum anneal temperature reported by Mohammadpour et al. in the liquid phase degradation of methylene blue [21].

In contrast to the CO_2 reduction results, the collapsed 680 °C sample did not show elevated reactivity relative to the other nanotube samples. One reason is that anatase in comparison to rutile is a more powerful oxidant than a reductant [28,34,44]. Thus, the decrease in surface area has a much greater effect on the rates of acetaldehyde oxidation than on CO_2 reduction. Another plausible reason is the difference in the relative adsorptive affinities among the nanotube composites; the anatase surface of the nanotubes may have greater affinity for acetaldehyde, but less affinity for CO_2 , than the 680 °C sample.

The nanotube samples were also probed for oxidative ability under visible light. The rate constants for acetaldehyde oxidation under 400 nm irradiation are given in Fig. 9. Similar to CO_2 reduction, visible reactivity depends on phase composition. Samples with a higher rutile content were more active under 400 nm illumination. The 620 °C sample (77% rutile) was the most reactive, with a rate constant of $9.02 \times 10^{-4} \text{ min}^{-1}$. Again, in contrast to CO_2 reduction (Fig. 6), the collapsed 680 °C sample did not exhibit enhanced

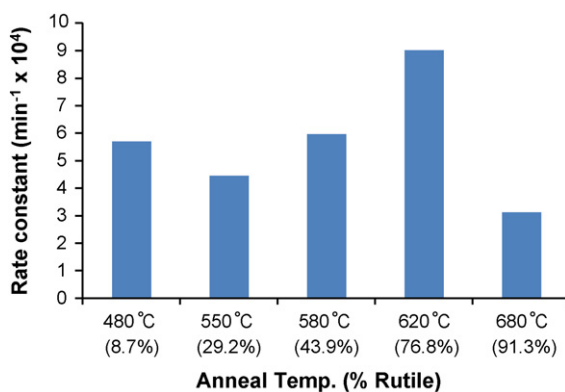


Fig. 9. Acetaldehyde oxidation first order apparent rate constants under 400 nm irradiation for TiNT arrays of varying anneal temperature.

reactivity relative to the nanotube samples. Overall, the rate constants for the nanotube samples are significantly lower under this condition (even considering the differences in lamp intensities), indicating that the oxidative reactivity of the nanotube arrays is not enhanced much under visible light. Whereas the highest rate of reduction under UV was only ~5 times greater than that under 400 nm irradiation, the highest rate of oxidation under UV is ~45 times greater than the highest under 400 nm. Thus, the red-shifted photoresponse caused by band gap narrowing in the TiNT samples enhances CO_2 reduction to a far greater extent than acetaldehyde oxidation.

4. Conclusions

The rutile phase composition of TiNT arrays formed by anodic oxidation in aqueous electrolytes is directly tunable by anneal temperature. Initially, rutile crystallites form in the base layer where nucleation and growth are not limited by volume constrictions present in the nanotube walls. Near 680 °C, the tube walls rupture as near complete conversion of anatase to rutile is achieved. Increasing the ratio of the rutile phase in the barrier layer extends the photoresponse of the material into the visible range, leading to increased light harvesting. This ability to tune photoresponse allows us to also optimize reactivity. Under visible and near visible light wavelengths, CO_2 reduction rates increased with sample anneal temperature/rutile content. With the exception of the collapsed nanotube composite (680 °C), under UV illumination this pattern was reversed; the photoreduction of CO_2 decreased with increasing anneal temperature, because anatase content is more critical for UV activation. Oxidative reactivity of the nanotube arrays behaved differently. Under UV, an optimum crystal phase ratio (which is common in most studies of mixed-phase TiO_2) was observed for the 550 °C sample which is 29% rutile. Except for the 620 °C/77% rutile sample, the oxidative reactivity under visible light was not significantly enhanced by increasing the rutile phase. Visible light oxidative reactivity was limited compared to visible light reductive activity. Interestingly, the collapsed, predominantly rutile nanotube sample exhibited comparable reactivity for CO_2 reduction to the uncollapsed samples under UV and visible light, despite the drastic loss in surface area of this collapsed structure. This is attributed to the creation of a material with an increased population of highly active anatase–rutile interfacial active sites absent in the regular nanotubes due to the segregation of the rutile and anatase phases.

We would like to note that the morphological properties of the nanotubes in this study were not optimized. In particular, the length and pore size of these nanotubes are also tunable and greatly variable (lengths in the 100 s of microns have been reported). In

addition, there is also potential for doping and co-catalyst loading of these arrays. There is still much work to be done to determine the optimum combination of these numerous factors for oxidative and reductive photocatalysis. Control of phase composition through annealing is an attractive way to tune the reactivity of titania nanotube arrays and extend their photoresponse to longer wavelengths.

Acknowledgements

This research was supported by a grant from the National Science Foundation (CBET-0829146). The SEM microscopy work was performed in the EPIC facility of NUANCE Center at Northwestern University. NUANCE Center is supported by NSF-NSEC, NSF-MRSEC, Keck Foundation, the State of Illinois, and Northwestern University. Also, we would like to thank the J.B. Cohen X-ray Diffraction Facility and the Keck Biophysics Facility of Northwestern where XRD and diffuse reflectance measurements were performed, respectively.

References

- [1] J.G. Jia, T. Ohno, Y. Masaki, M. Matsumura, Chemistry Letters (1999) 963–964.
- [2] A.G. Agrios, K.A. Gray, E. Weitz, Langmuir 20 (2004) 5911–5917.
- [3] M.A. Fox, M.T. Dulay, Chemical Reviews 93 (1993) 341–357.
- [4] A.P. Rivera, K. Tanaka, T. Hisanaga, Applied Catalysis B: Environmental 3 (1993) 37–44.
- [5] J.M. Herrmann, J. Disdier, P. Pichat, S. Malato, J. Blanco, Applied Catalysis B: Environmental 17 (1998) 15–23.
- [6] S. Ciston, R.M. Luetow, K.A. Gray, Journal of Membrane Science 320 (2008) 101–107.
- [7] A.M. Ruiz, G. Sakai, A. Cornet, K. Shimano, J.R. Morante, N. Yamazoe, Sensors and Actuators B: Chemical 93 (2003) 509–518.
- [8] L.R. Skubal, N.K. Meshkov, M.C. Vogt, Journal of Photochemistry and Photobiology A: Chemistry 148 (2002) 103–108.
- [9] R. Blossey, Nature Materials 2 (2003) 301–306.
- [10] K.H. Guan, Surface & Coatings Technology 191 (2005) 155–160.
- [11] D. Gong, C.A. Grimes, O.K. Varghese, W.C. Hu, R.S. Singh, Z. Chen, E.C. Dickey, Journal of Materials Research 16 (2001) 3331–3334.
- [12] Q. Cai, M. Paulose, O.K. Varghese, C.A. Grimes, Journal of Materials Research 20 (2005) 7.
- [13] K. Zhu, N.R. Neale, A. Miedaner, A.J. Frank, Nano Letters 7 (2007) 69–74.
- [14] M. Paulose, K. Shankar, O.K. Varghese, G.K. Mor, C.A. Grimes, Journal of Physics D: Applied Physics 39 (2006) 2498–2503.
- [15] O.K. Varghese, D.W. Gong, M. Paulose, K.G. Ong, E.C. Dickey, C.A. Grimes, Advanced Materials 15 (2003) 624–627.
- [16] J.M. Macak, H. Tsuchiya, A. Ghicov, K. Yasuda, R. Hahn, S. Bauer, P. Schmuki, Current Opinion in Solid State & Materials Science 11 (2007) 3–18.
- [17] Z. Liu, X. Zhang, S. Nishimoto, T. Murakami, A. Fujishima, Environmental Science & Technology 42 (2008) 5.
- [18] S.S. Malwadkar, R.S. Gholap, S.V. Awate, P.V. Korake, M.G. Chaskar, N.M. Gupta, Journal of Photochemistry and Photobiology A: Chemistry 203 (2009) 24–31.
- [19] I. Paramasivam, J.M. Macak, A. Ghicov, P. Schmuki, Chemical Physics Letters 445 (2007) 5.
- [20] H.F. Zhuang, C.J. Lin, Y.K. Lai, L. Sun, J. Li, Environmental Science & Technology 41 (2007) 4735–4740.
- [21] R. Mohammadpour, A.I. Zad, M.M. Ahadian, N. Taghavinia, A. Dolati, European Physical Journal: Applied Physics 47 (2009) 7.
- [22] Y.K. Lai, L. Sun, Y.C. Chen, H.F. Zhuang, C.J. Lin, J.W. Chin, Journal of the Electrochemical Society 153 (2006) D123–D127.
- [23] Q.D. Zhao, X.Y. Li, N. Wang, Y. Hou, X. Quan, G.H. Chen, Journal of Nanoparticle Research 11 (2009) 2153–2161.
- [24] Z. Liu, X. Zhang, S. Nishimoto, M. Jin, D.A. Tryk, T. Murakami, A. Fujishima, The Journal of Physical Chemistry C 112 (2007) 253–259.
- [25] O.K. Varghese, M. Paulose, T.J. LaTempa, C.A. Grimes, Nano Letters 9 (2009) 731–737.
- [26] D.C. Hurun, A.G. Agrios, K.A. Gray, T. Rajh, M.C. Thurnauer, Journal of Physical Chemistry B 107 (2003) 4545–4549.
- [27] T. Sumita, T. Yamaki, S. Yamamoto, A. Miyashita, Applied Surface Science 200 (2002) 21–26.
- [28] G. Riegel, J.R. Bolton, Journal of Physical Chemistry 99 (1995) 4215–4224.
- [29] Q. Shen, K. Katayama, T. Sawada, M. Yamaguchi, Y. Kumagai, T. Toyoda, Chemical Physics Letters 419 (2006) 5.
- [30] G. Li, K.A. Gray, Chemical Physics 339 (2007) 15.
- [31] T. Ohno, K. Tokieda, S. Higashida, M. Matsumura, Applied Catalysis A: General 244 (2003) 383–391.
- [32] S. Bakardjieva, J. Subrt, V. Stengl, M.J. Dianez, M.J. Sayagues, Applied Catalysis B: Environmental 58 (2005) 193–202.
- [33] L. Chen, Civil and Environmental Engineering, Northwestern University, Evanston, IL, 2008.

- [34] G. Li, S. Ciston, Z.V. Saponjic, L. Chen, N.M. Dimitrijevic, T. Rajh, K.A. Gray, *Journal of Catalysis* 253 (2008) 6.
- [35] D.C. Hurum, K.A. Gray, T. Rajh, M.C. Thurnauer, *Journal of Physical Chemistry B* 109 (2005) 977–980.
- [36] M. Anpo, H. Yamashita, K. Ikeue, Y. Fujii, S.G. Zhang, Y. Ichihashi, D.R. Park, Y. Suzuki, K. Koyano, T. Tatsumi, *Catalysis Today* 44 (1998) 6.
- [37] L. Chen, P.A. DeSario, M.E. Graham, K.A. Gray, *Applied Surface Science* (2010), in review.
- [38] O.K. Varghese, D.W. Gong, M. Paulose, C.A. Grimes, E.C. Dickey, *Journal of Materials Research* 18 (2003) 156–165.
- [39] H.Z. Zhang, J.F. Banfield, *Journal of Materials Research* 15 (2000) 437–448.
- [40] P.I. Gouma, M.J. Mills, *Journal of the American Ceramic Society* 84 (2001) 4.
- [41] R.A. Spurr, H. Myers, *Analytical Chemistry* 29 (1957) 760–762.
- [42] G. Li, N.M. Dimitrijevic, L. Chen, J.M. Nichols, T. Rajh, K.A. Gray, *Journal of the American Chemical Society* 130 (2008) 2.
- [43] J. Zhang, M. Li, Z. Feng, J. Chen, C. Li, *The Journal of Physical Chemistry B, Condensed Matter, Materials, Surfaces, Interfaces & Biophysical* 110 (2006) 927–935.
- [44] G. Cappelletti, C.L. Bianchi, S. Ardizzone, *Applied Catalysis B: Environmental* 78 (2008) 193–201.